



Maps of Tethys' thermophysical properties

C.J.A. Howett^{a,*}, J.R. Spencer^a, T. Hurford^b, A. Verbiscer^c, M. Segura^b

^a Southwest Research Institute, 1050 Walnut Street, Suite 300, Boulder, CO 80302, USA

^b Goddard Space Flight Center, Maryland, USA

^c University of Virginia, Virginia, USA

ABSTRACT

On 11th April 2015 Cassini's Composite Infrared Spectrometer (CIRS) made a series of observations of Tethys' daytime anti-Saturn hemisphere over a nine-hour time period. During this time the sub-spacecraft position was remarkably stable (0.3° S to 3.9° S; 153.2° W to 221.8° W), and so these observations provide unprecedented coverage of diurnal temperature variations on Tethys' anti-Saturn hemisphere. In 2012 a thermal anomaly was discovered at low latitudes on Tethys' leading hemisphere; it appears cooler during the day and warmer at night than its surroundings (Howett et al., 2012) and is spatially correlated with a decrease in the IR3/UV3 visible color ratio (Schenk et al., 2011). The cause of this anomaly is believed to be surface alteration by high-energy electrons, which preferentially bombard low-latitudes of Tethys' leading hemisphere (Schenk et al., 2011; Howett et al., 2012; Paranicas et al. 2014; Schaible et al., 2017). The thermal anomaly was quickly dubbed "Pac-Man" due to its resemblance to the 1980s video game icon. We use these daytime 2015 CIRS data, along with two sets of nighttime CIRS observations of Tethys (from 27 June 2007 and 17 August 2015) to make maps of bolometric Bond albedo and thermal inertia variations across the anti-Saturn hemisphere of Tethys (including the edge of its Pac-Man region). These maps confirm the presence of the Pac-Man thermal anomaly and show that while Tethys' bolometric Bond albedo varies negligibly outside and inside the anomaly (0.69 ± 0.02 inside, compared to 0.71 ± 0.04 outside) the thermal inertia varies dramatically ($29 \pm 10 \text{ J m}^{-2} \text{ K}^{-1} \text{ s}^{-1/2}$ inside, compared to $9 \pm 4 \text{ J m}^{-2} \text{ K}^{-1} \text{ s}^{-1/2}$ outside). These thermal inertias are in keeping with previously published values: $25 \pm 3 \text{ J m}^{-2} \text{ K}^{-1} \text{ s}^{-1/2}$ inside, and $5 \pm 1 \text{ J m}^{-2} \text{ K}^{-1} \text{ s}^{-1/2}$ outside the anomaly (Howett et al., 2012).

A detailed analysis shows that on smaller spatial-scales the bolometric Bond albedo does vary: increasing to a peak value at 180° W. For longitudes between $\sim 100^\circ$ W and $\sim 160^\circ$ W the thermal inertia increases from northern to southern latitudes, while the reverse is true for bolometric Bond albedo. The thermal inertia on Tethys generally increases towards the center of its leading hemisphere but also displays other notable small-scale variations. These thermal inertia and bolometric Bond albedo variations are perhaps due to differences in competing surface modification by E ring grains and high-energy electrons which both bombard Tethys' leading hemisphere (but in different ways). A comparison between the observed temperatures and our best thermal model fits shows notable discrepancies in the morning warming curve, which may provide evidence of regional variations in surface roughness effects, perhaps again due to variations in surface alteration mechanisms.

1. Introduction

Voyager observations of Tethys at visible wavelengths showed a relatively dark region at low latitudes on Tethys' leading hemisphere (Stooke, 1989, 2002). Cassini observations of Tethys acquired early in the mission by its Imaging Science Subsystem (ISS) showed that this region was 2–3% brighter in the Narrow Angle Camera (NAC) UV3 filter (338 nm) and 8% darker in the NAC IR3 (930 nm) filter (Elder et al., 2007) than its surroundings. A larger systematic study of the visible color of Saturn's major icy satellites confirmed that this region is darker than its surroundings in IR3/UV3 color ratio maps (930 nm/338 nm) (Schenk et al., 2011). In this map, Tethys' equatorial band does not appear evenly colored, but rather it is brightest close to the equator and darkest near its southern margin. Observations of Tethys (and Mimas) made by Cassini's Composite Infrared Spectrometer (CIRS) showed that the observed visible color anomalies were spatially correlated with a region of anomalously high thermal inertia (Howett

et al., 2011, 2012). Although Tethys' color and thermal inertia anomaly are similar to those on Mimas they have a smaller latitudinal extent and smaller temperature contrast (Howett et al., 2011; Schenk et al., 2011). These thermal anomalies were quickly dubbed "PacMen" because from certain angles they resemble the shape of the 1980's video game icon.

Surfaces inside these anomalous regions are cooler during the daytime, and warmer at night, due to higher thermal inertia inside of the anomalous region than that of its surroundings (Howett et al., 2011, 2012). Thermal inertia describes how a surface is able to store and release thermal energy and is defined as $\sqrt{k\rho c}$, where k is thermal conductivity ($\text{J s}^{-1} \text{ m}^{-1} \text{ K}^{-1}$), ρ is the bulk density (kg m^{-3}), and c is specific heat capacity ($\text{J K}^{-1} \text{ kg}^{-1}$). The units of thermal inertia are $\text{J m}^{-2} \text{ K}^{-1} \text{ s}^{-1/2}$, which we abbreviate as MKS. The thermal inertia of Tethys (Mimas) was 25 ± 3 MKS (66 ± 23 MKS) inside the anomalous region and 5 ± 1 MKS (< 16 MKS) outside of it (Howett et al., 2011, 2012). Interestingly a similar thermal anomaly was discovered close to the equator on Dione's leading hemisphere without a

* Corresponding author.

E-mail address: howett@boulder.swri.edu (C.J.A. Howett).

corresponding color anomaly (Howett et al., 2014). Dione's thermal anomaly is smaller in magnitude (11 MKS, compared to a background value of 8 MKS), implying a smaller degree of surface alteration than on Mimas and Tethys.

Results from Cassini's Magnetospheric Imaging Instrument's (MIMI) mission-averaged electron energy spectra show high-energy electrons preferentially bombard low latitudes on the leading hemispheres of Mimas, Tethys and Dione (Paranicas et al., 2014). The location of this bombardment is also spatially correlated with the color and thermal anomalies (Schenk et al., 2011; Howett et al., 2011, 2012, 2014). It is likely that these high-energy electrons are the cause of the color and thermal anomalies: electrons mobilize water molecules in their path, and these water molecules recondense at grain contacts. This mobilization increases the contact area between the grains, increasing their thermal conductivity and hence thermal inertia. In essence, the grains are better glued together (Schenk et al., 2011; Howett et al., 2011; Schaible et al., 2017).

High-energy electrons aren't the only things that bombard Tethys' surface. E ring grains, which are expected to be almost pure water ice, bombard Tethys' leading hemisphere (Hamilton and Burns, 1994), peak at longitudes ~30° and 175° W (Fig. 1, Kempf et al., 2018). E ring grains are expected to brighten Tethys' surface as they bombard it by "sand-blasting" the surface, thereby coating the surface with fresh ice grains (Hamilton and Burns, 1994; Shkuratov and Helfenstein, 2001; Verbiscer et al., 2007). This brightening is believed to be the cause of the well-documented visible albedo asymmetry between Tethys' brighter-leading and darker-trailing hemispheres (e.g. Buratti and Veverka, 1984; Schenk et al., 2011). E ring grains also affect a surface's UV absorption: by combining observations made by the Hubble Space Telescope's Space Telescope Imaging Spectrometer (STIS), Cassini's Visual and Infrared Mapping Spectrometer (VIMS), and its Ultraviolet Imaging Spectrograph (UVIS) it was shown that the UV absorption strength (defined as the ratio of the geometric albedo at 300 nm and 600 nm) on Tethys is anti-correlated with E ring grain flux (Hendrix et al., 2018).

The data used here were taken by Cassini's Composite Infrared Spectrometer (CIRS), (Flasar et al., 2004). CIRS is a Fourier transform spectrometer with three focal planes, covering 10–1400 cm⁻¹ (7.1–1000 μm). Wavenumbers between 10 and 600 cm⁻¹ (9.1–1000 μm) are detected by focal plane 1 (FP1), which has a spatial resolution of 3.9 mrad. Higher wavenumbers, between 600 and 1100 cm⁻¹ (9.1–16.7 μm) and 1100–1400 cm⁻¹ (7.1–9.1 μm) are detected by focal planes 3 and 4 respectively (FP3 and FP4). These two focal planes each have a row of ten detectors, each of which has a 0.273 by 0.273 mrad field of view. The different wavelength ranges of the focal planes make them sensitive to different temperature regimes. FP1 is sensitive to both daytime and nighttime surface temperatures of the icy Saturnian satellites. The sensitivity of FP4 to the surface temperatures of the icy Saturnian satellites is too low to be of use, except across

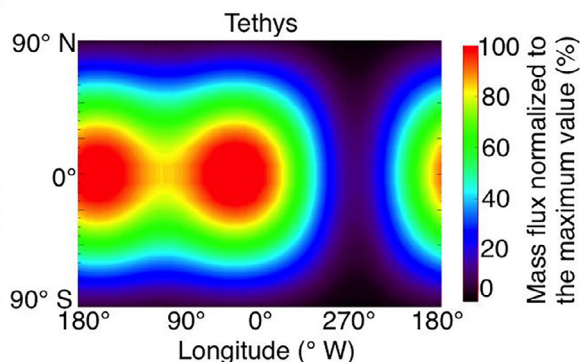


Fig. 1. The mass influx map for Tethys from Kempf et al., (2018).

Table 1

Summary of the CIRS data analyzed in this work. The first seven observations in Rev 214 describe the full hemisphere scans used in Fig. 1, while the bottom two (below the double line) are the smaller spatial-scale scans taken in the same encounter. All data taken Revs 47 and 220 were made using FP1, while those in Rev 214 were made by FP3. Due to the higher number of detectors of FP3 compared to FP1 many more observations were taken per scan when FP3 is used. Due to space constraints a number of abbreviations are used: "Num. of Obs." Indicates the number of individual CIRS spectra that were taken during each scan, "Sub-scf" point describes the sub-spacecraft point.

Spacecraft Clock Start Time	Spacecraft Clock End Time	Start Time (UTC)	End Time (UTC)	Num. of Obs.	Range at Start (km)	Range at End (km)	Sub-scf point at Start (Lon/Lat)	Sub-scf point at End (Lon/Lat)	Sub-solar point at Start (Lon/Lat)	Sub-solar point at End (Lon/Lat)
Rev 47 (27 Jun 2007)										
1,182,967,861	1,182,969,207	18:12:00	18:29:54	68	61,560	46,942	157.7° W/19.0° N	157.8° W/23.8° N	307.2° W/12.9° S	310.2° W/12.9° S
Rev 214 (11 Apr 2015)										
1,428,728,646	1,428,731,408	05:04:06	05:50:08	1338	238,246	214,753	153.2° W/0.3° S	158.9° W/0.5° S	130.9° W/24.1° N	137.0° W/24.1° N
1,428,734,953	1,428,736,988	06:49:13	07:23:08	1146	187,475	173,291	166.5° W/0.7° S	170.9° W/0.9° S	144.7° W/24.1° N	149.2° W/24.1° N
1,428,737,466	1,428,739,599	07:31:06	08:06:39	1379	170,113	156,655	172.0° W/0.9° S	176.8° W/1.1° S	150.2° W/24.1° N	154.8° W/24.1° N
1,428,740,058	1,428,742,369	08:14:18	08:52:49	1617	153,911	140,875	177.9° W/1.2° S	183.2° W/1.4° S	155.8° W/24.1° N	160.8° W/24.1° N
1,428,743,125	1,428,745,687	09:05:25	09:48:07	1768	136,888	124,362	185.0° W/1.5° S	190.9° W/1.7° S	162.4° W/24.1° N	167.9° W/24.1° N
1,428,749,568	1,428,755,121	10:52:48	12:25:21	3804	108,028	89,204	199.9° W/2.2° S	211.6° W/2.9° S	176.2° W/24.1° N	188.0° W/24.1° N
1,428,755,621	1,428,761,789	12:33:41	14:16:29	4247	87,724	71,705	212.5° W/3.0° S	221.8° W/3.9° S	189.1° W/24.1° N	202.3° W/24.1° N
Rev 220 (17 Aug 2015)										
1,439,850,656	1,439,851,403	22:30:56	22:43:23	78	44,332	45,853	98.1° W/5.6° S	94.0° W/5.3° S	193.3° W/24.3° N	194.9° W/24.3° N

the active regions of Enceladus and Iapetus' dark warmer surfaces. FP3 is sensitive to temperatures >65 K, making it suitable to detect the daytime temperatures on most of Saturn's satellites (including Tethys), and so FP3 often presents the best trade between signal to noise ratio and spatial resolution for these types of observations. Due to these limitations we use FP3 for daytime observations and FP1 for nighttime ones.

2. Data analysis and results

On 11th April 2015 during Cassini's 214th rev of Saturn CIRS took a series of seven scans of Tethys' daytime anti-Saturn hemisphere as Cassini approached the target, detailed in Table 1. As the table shows, during the time of the observations the sub-spacecraft position was remarkably stable (0.3° S to 3.9° S; 153.2° W to 221.8° W). This meant that for the entire observation (approximately nine hours) CIRS was viewing much of the same anti-Saturn and leading hemisphere of Tethys, providing an unprecedented view of surface temperature changes with local time for multiple surface locations. During this time CIRS almost continually scanned its FP3 detector across Tethys, interrupted only to allow observations by other Cassini remote sensing instruments to be made. In order to use these daytime data to constrain Tethys' thermophysical properties, nighttime observations must also be used in conjunction with these daytime data to provide the required constraint. We use two sets of CIRS FP1 nighttime observations of Tethys' leading hemisphere taken on 27 June 2007 (Rev 47) and 17 August 2015 (Rev 220). The details of these observations are also given in Table 1. As the table shows, these nighttime observations are taken closer to Tethys (vital to obtain high-spatial resolution observations with FP1 because its field of view is larger than that of FP3, which was used for the daytime observations).

To compare these data, each scan in Table 1 was rebinned into 5° by 5° latitude and longitude bins, averaging radiances for all observations in the scan falling in each bin. The radiance of each bin is then converted to a temperature by finding the best-fitting blackbody temperature curve to the bin's radiance using IDL's amoeba algorithm (a downhill simplex method based on the work of Nelder and Mead (1965)), to minimize the chi-squared statistic assuming the noise to be 1% of the maximum value of the observed radiance, and that the surface emits as a blackbody. The noise on the determined surface temperatures is derived using a two-step Monte Carlo technique: first a synthetic noise with a comparable magnitude to the observed noise is created and added to the previously determined best fitting blackbody curve. Then this spectrum is fitted by a blackbody emission spectrum. This process is repeated numerous times, and the temperature error estimate is given by the standard deviation of the temperatures whose blackbody emission spectra are able to fit the created spectra. This technique was then repeated for all sets of observations to produce the surface temperatures shown in Figs. 2 (daytime) and 3 (nighttime).

We then follow the same technique that Howett et al. (2014) used to produce bolometric Bond albedo and thermal inertia maps of Rhea and Dione to make a similar set of maps for Tethys. Model diurnal temperatures were pre-calculated for each encounter (i.e. for a specific target rotation speed, latitude, local time, sub-solar latitude and heliocentric distance) by a simple diurnal 1-D thermal model (c.f. Spencer, 1989). So while the model is a diurnal model the seasonal variation in heliocentric distance and sub-solar latitude are accounted for. The model assumes a unit emissivity and does not include heating from Saturn or reflected sunlight from Saturn. The model also does not include the effect of eclipses, since Tethys' 'eclipse season' lies outside of these observation times; the times of Tethys' eclipses were calculated using NASA's standard Navigation and Ancillary Information Facility (NAIF) SPICE kernels de430.bsp and sat359l.bsp and routine gfoct (Acton, 1996), and it was determined that Tethys' eclipse season lasted from October 2007 to October 2011. The model was run for a range of thermal inertias and bolometric Bond albedos: thermal inertias between

1 and 200 MKS in 1 MKS increments, and bolometric Bond albedos between 0.30 and 0.80 in 0.01 increments were sampled.

For each CIRS observation, the modeled surface temperatures were then compared to those determined from the data using the following steps. Step 1) for each observation the reduced chi-squared value was separately determined for each bin that was covered. This produced a metric for how well the temperatures predicted by different combinations of bolometric Bond albedo and thermal inertia compared to those determined from CIRS data. Step 2) for each bin the mean reduced chi-squared value was calculated using all the pre-calculated reduced chi-squared values for all observations that covered that bin. This determines the combinations of thermal inertia and bolometric Bond albedo values that are able to fit *all* the observations of a given bin. A bolometric Bond albedo and thermal inertia combination is assumed to be consistent with the data if it produces a mean reduced chi-squared under unity. Step 3) for each bin the mean value of the consistent bolometric Bond albedo and thermal inertias were assumed for the bin's values, and their standard deviation is reported as the bin's error. The maps of bolometric Bond albedo, thermal inertia and their standard deviations, produced using this technique, are shown in Fig. 4.

3. Discussion

The temperature maps of Tethys clearly show that the surface does not respond uniformly to solar forcing. As Fig. 2 shows the temperature surrounding the sub-solar point (indicated by the white dots) increases dramatically as it moves from Tethys' leading to trailing hemisphere. This pattern isn't surprising, as we know the thermal inertia of Tethys' leading hemisphere is notably higher than that of its trailing one (Howett et al., 2012), resulting in lower daytime (and warmer nighttime) temperatures. However, this effect is remarkably clear in this unprecedented observation of local time change on Tethys. What can be inferred from the temperature maps is shown clearly in Tethys' thermophysical property maps (Fig. 4): Tethys has a high thermal inertia at low latitudes on its leading hemisphere and a bright leading hemisphere.

The bolometric Bond albedo of Tethys' leading hemisphere is 0.70 ± 0.03 , which is a bright surface for an icy satellite (Europa's global bolometric Bond albedo is 0.55 (Spencer et al., 1999), Mimas' is <0.53 and Enceladus' is 0.81 ± 0.04 (Howett et al., 2010)). Assuming the thermally anomalous region is bounded by the 10^5 MeV $\text{cm}^{-2} \text{s}^{-1}$ contour shown in Fig. 2 and the "surroundings" are defined as everything outside of the 10^3 MeV $\text{cm}^{-2} \text{s}^{-1}$ contour on Tethys' leading hemisphere, then the mean bolometric Bond albedo is 0.69 ± 0.02 inside the anomalous region and 0.71 ± 0.04 outside. While these bolometric Bond albedo values agree (within their uncertainty) the albedo does differ on regional scales, as discussed further below.

The map of Tethys' thermal inertia shows a general trend of high values occurring close to the equator and gradually decreasing towards higher latitudes (smaller-spatial scale thermal inertia variations are also discussed below). Using the same definition of the anomaly boundary as outlined above, the thermal inertia inside the anomaly is 29 ± 10 MKS and 9 ± 4 MKS outside. The lens shape of the anomalous region is clearly visible in the maps towards the anti-Saturn apex, where its latitudinal extent is notably narrower than at the center of the leading hemisphere. Also shown in Fig. 4 is the IR3/UV3 (930 nm/338 nm) color ratio map of Tethys, derived from Cassini Imaging Subsystem (ISS) images by Schenk et al. (2011) and contours of electron energy flux bombarding Tethys' surface (in units of \log_{10} MeV $\text{cm}^{-2} \text{s}^{-1}$, from Paranicas et al., 2014). The spatial correlation between the location of the dark IR3/UV3 lens and the region of high thermal inertia can clearly be seen and also the non-uniform coloration of the lens (Howett et al., 2012; Schenk et al., 2011). It's possible that the decrease in mass influx of E ring grains that occurs on the leading hemisphere between the peaks (i.e. around 90° W) is the reason the IR/UV color ratio is less dark here than towards $\sim 180^\circ$ and 0° W (Figs. 1 and 4, Schenk et al.,

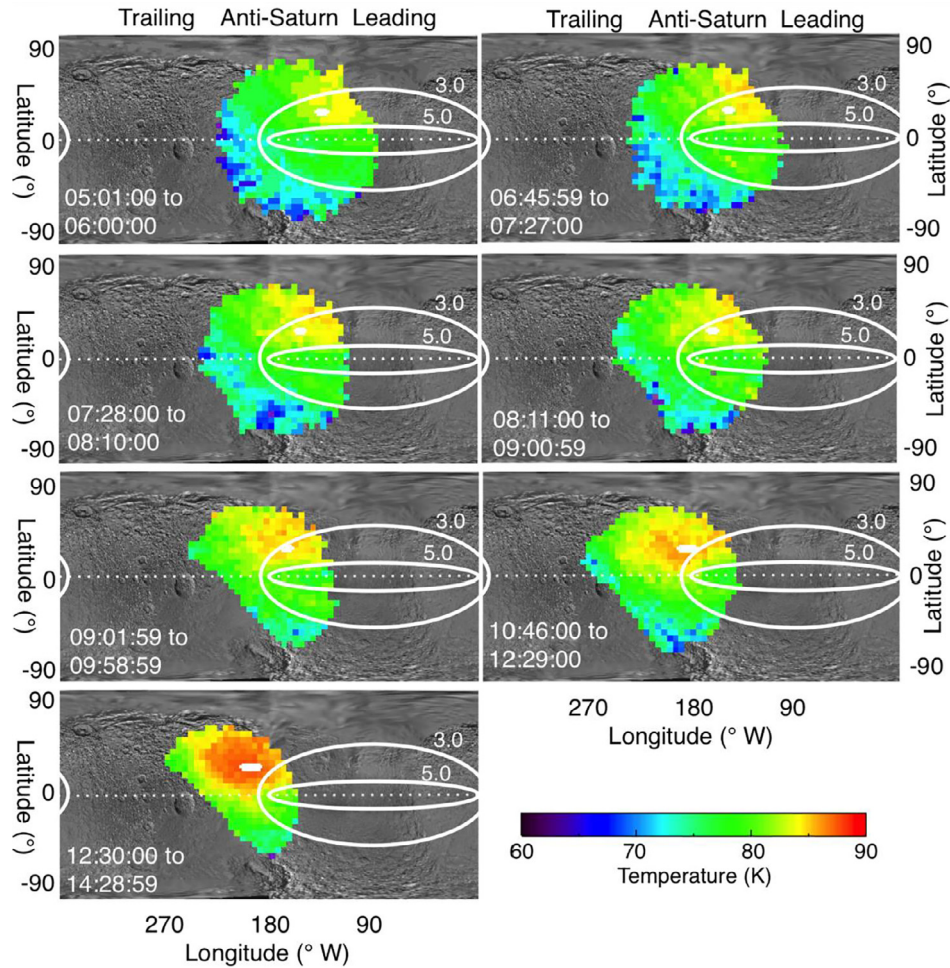


Fig. 2. Daytime surface temperature maps of Tethys derived from Cassini Rev 214 FP3 scans taken on 11th April 2015. Times of each scan are shown in the subfigures. The contours describe the predicted electron energy flux onto Tethys’ surface, in units of $\log_{10}(\text{MeV cm}^{-2} \text{s}^{-1})$. The white spots in the center of the image show the location of the sub-solar position during the time of the scan. The background map is Planetary Image Atlas (PIA) 14931, white-dotted horizontal line indicates the position of 0° N.

2011; Kempf et al., 2018).

The bolometric Bond albedo and thermal inertia variation with longitude at 20° S, 10° S, 0° N, 10° N, and 20° N latitude are given in Fig. 5. Note the position given is for the southern or western edge of the 5° bins, not at the center of bins (e.g. the bin described by 20° S extends from 20° S to 15° S). For reference, the ± 10° latitude lines lie just equatorward of the inner contour shown on the Fig. 4 maps, and the ± 20° latitude lines lie just outside of it. Fig. 5 shows that from

~200° W to 160° W the bolometric Bond albedos at all latitudes generally agree, and seem to increase towards a peak at 180° W. In the same region the thermal inertias at all latitudes gradually increases with decreasing longitudes.

Fig. 5 also shows a more complex picture for variations in bolometric Bond albedo and thermal inertia variation between longitudes ~160° W and 100° W. Here the bolometric Bond albedo and thermal inertia show a north-south asymmetry: albedos increase from southern

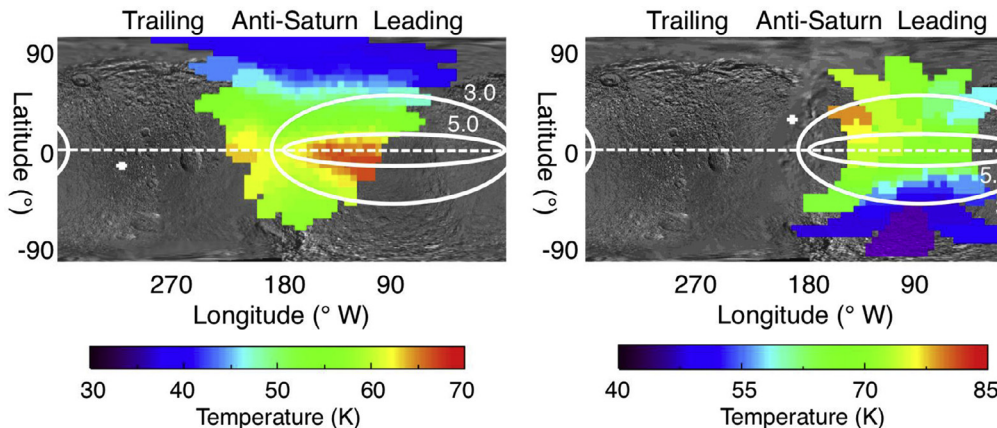


Fig. 3. Nighttime surface temperatures of Tethys derived from CIRS FP1 observations taken during Cassini Revs 47 and 220. The contours are the same as described in Fig. 1, and the white cross shows the location of the sub-solar point at the time of the scan. The background map is Planetary Image Atlas (PIA) 14931, white-dotted horizontal line indicates the position of 0° N. (a) Rev 47 data, taken from 18:11:00 to 18:33:00 UTC on 27th June 2007. (b) Rev 220 data, taken from 22:29:54 to 22:48:30 UTC on 17th August 2015.

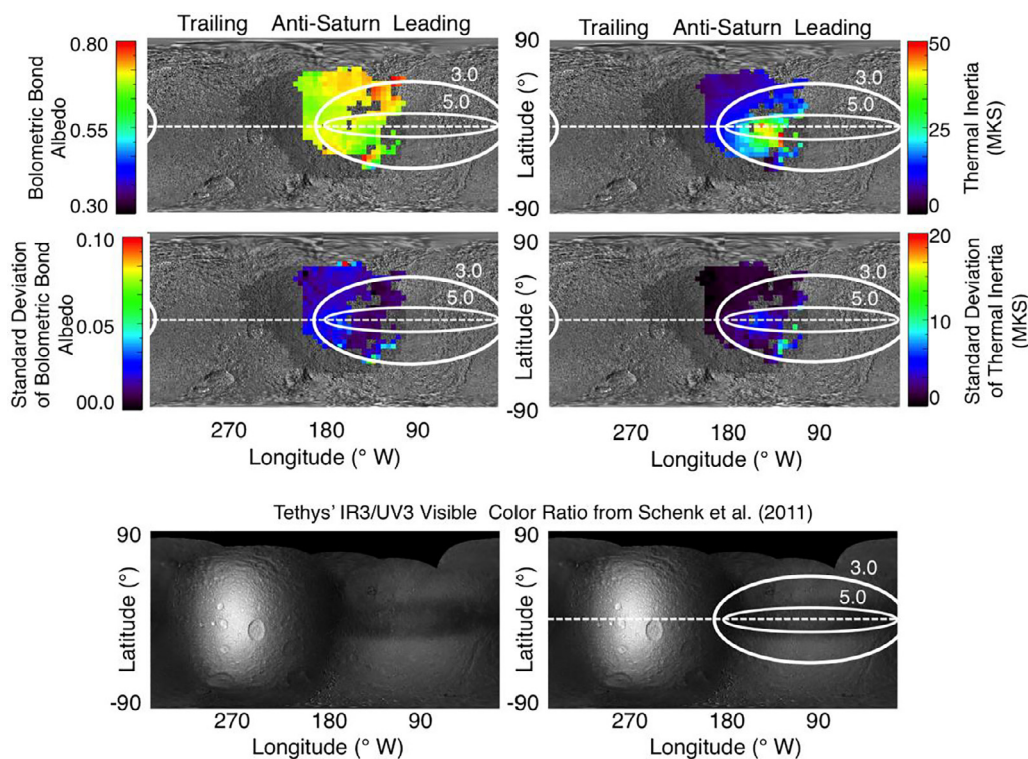


Fig. 4. Maps of Tethys' thermal inertia and bolometric Bond albedo, with their standard deviations. The darker grey areas indicate where CIRS had coverage, but not enough to provide adequate constraints on the surface's thermophysical properties. The contours describe the predicted electron energy flux onto Tethys' surface. They show the predicted electron energy flux onto Tethys' surface, in units of $\log_{10}(\text{MeV cm}^{-2} \text{s}^{-1})$. The basemap on all images is PIA 14931, with the exception of the bottom maps, which show the IR3/UV3 color ratio (930 nm/338 nm) map for Tethys from Schenk et al. (2011). The white-dotted horizontal line on sub-figures indicates the position of 0° N. Note, the bottom two maps are identical except the right-hand one has the equator and electron flux contours overlaid, the left-hand one is kept clear so the details of the map can be seen.

to northern latitudes, while thermal inertia generally increases from northern to southern ones. Inspection of the temperature maps shows that this north-south asymmetry is most apparent in the nighttime temperature map produced by the Rev 47 data, manifesting as warmer nighttime temperatures in the southern hemisphere. In the same longitude region, different patterns of bolometric Bond albedo and thermal inertia variation are seen at different latitudes. With the exception of the one data point at 125° W, the bolometric Bond albedo values at equatorial and southern latitudes increase towards ~180° W. If all data points are considered, then only those at the equator follow this pattern, and those at southern latitudes follow a more complex one. The bolometric Bond albedo at latitudes 10° and 20° N follow a very different pattern: increasing from ~180° W to ~120° W before decreasing again. In the same region, in the northern hemisphere, thermal inertia generally increases towards the apex of Tethys' leading hemisphere (90° W). Again, with the exception of one data point (at 105° W) it's feasible that thermal inertia variations at 20° S also follow the same pattern. However, the thermal inertia variation at the equator and 10° S follow quite a different pattern, appearing to increase to ~145° W and then decreasing again. Frustratingly, CIRS does not have sufficient day and nighttime longitude coverage to derive thermal inertia at more easterly longitudes, so we don't know if the thermal inertia increases again towards 90° W, continue to decrease, or follow a different pattern entirely. We note that CIRS does have daytime coverage of this region (taken in September 2011, and presented in Howett et al., 2012) which shows the thermally anomalous region to continue to 0° W, but these data alone do not provide the diurnal coverage required to derive the thermophysical properties in this region.

The cause of the north-south albedo and thermal inertia asymmetry and the variation of bolometric Bond albedo and thermal inertia with longitude are unknown. The general trend of increasing albedo towards ~180° W is consistent with E ring grains preferentially bombarding and brightening the regions around 175° W (Fig. 1, Kempf et al., 2018). However, E ring grains are also predicted to bombard Tethys' leading hemisphere at 30° W (Fig. 1, Kempf et al., 2018), which could partially explain why the bolometric Bond albedo of Tethys' leading hemisphere has a complex pattern. E ring grain bombardment is predicted to be

symmetrical about the equator, so this bombardment doesn't explain why the bolometric Bond albedo in Tethys' leading northern and southern hemispheres differ. The contours in Fig. 2 show for non-equatorial latitudes the flux of high-energy electrons increases towards the apex of Tethys' leading hemisphere, which could explain the general increase in thermal inertia from ~200° W to 110° W. However the figure also shows that the high-energy electron flux bombarding Tethys is also symmetrical around its equator (c.f. Paranicas et al., 2014), so it is surprising that the changes in thermal inertia at latitudes 10° S and 20° S do not follow similar patterns of their northern counterparts.

The offset in the temperature maps is unlikely explained by errors in the pointing of the spacecraft and instrument, because the shift would have to be very large (~45 km at Tethys' equator), and affect all three observations similarly (or at least the Rev 47 and 214 data, which are the main drivers of the thermophysical property maps due to their higher spatial resolution). A pointing error also wouldn't explain why the offset is present in the daytime surface temperature maps of Tethys (where the anomaly is visible as a patch of cooler daytime temperatures) produced from interpretation of temperature-sensitive NIR spectral features in Cassini's Visual Infrared Mapping Spectrometer (VIMS) data (Filacchione et al., 2016). Or why Tethys' IR3/UV3 visible color ratio map also isn't symmetrical about the equator: the anomalous region appears darker in the southern hemisphere than in the northern one (and brightest at the equator) (Schenk et al., 2011). A more likely explanation is that the offset is real, and for some reason the southern part of the Pac-Man anomaly on Tethys has a higher thermal inertia, darker bolometric Bond albedo, and darker IR3/UV3 visible color ratio than its northern counterpart (and Tethys' equator is brighter in IR3/UV3 visible color and follows a different thermal inertia pattern). Albedo and thermal inertia variations along the equator are particularly interesting since at this latitude the flux of the high-energy electrons is expected to be uniform with longitude, but the E ring grain bombardment varies (Paranicas et al., 2014; Kempf et al., 2018). Perhaps high-energy electron flux or E ring grain bombardment is not uniform around Tethys' equator, or the surface in the southern hemisphere is more easily modified, perhaps due to different underlying geology (e.g. the region east of Odysseus crater on Tethys' leading hemisphere that

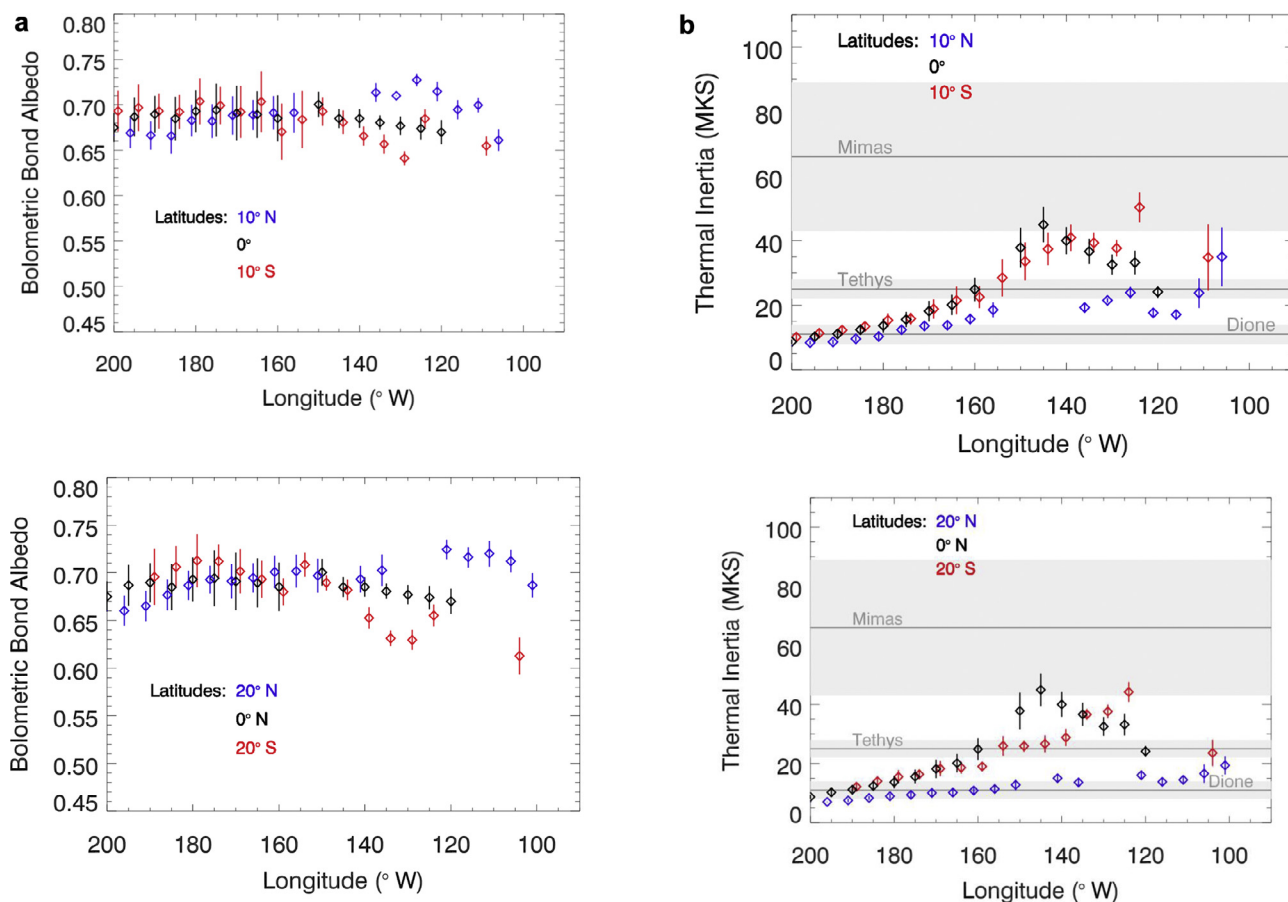


Fig. 5. Bolometric Bond albedo and thermal inertia variations with local time and latitude. In both subfigures values are given at: 20° S, 0° and 20° N latitudes, and the error bars show $\pm 1\sigma$ uncertainty. For reference the $\pm 10^\circ$ latitude lies just inside of the inner contour shown on the maps in Figs. 1–3, and $\pm 20^\circ$ latitude lies just outside of it. (a) Best fit bolometric Bond albedo variation with local time and latitude. (b) Best fit thermal inertia variation with local time and latitude. The previously published thermal inertia inside the thermal anomalies of Mimas, Tethys and Dione are indicated by the grey lines, and their uncertainties by the grey shading (c.f. Howett et al., 2011, 2012 and 2014).

runs north-east to south-west appears smoother than its surroundings), or southern hemisphere summer (which covered approximately 1995 to 2009 with equinox in 2003) caused sintering of the ice there increasing its thermal inertia. Or perhaps we are seeing the competing effects of surface alteration by E ring grain bombardment, surface modification by high-energy electrons, or other less-energetic species (e.g. neutrals) (which is again hard to explain since they are all believed to bombard Tethys symmetrically around its equator).

Fig. 6 shows the best fitting diurnal curves to the observed surface temperatures for different latitude/longitude positions on Tethys. For bins without an acceptable fit, the values that produced the best fit to data at 200° W/10° S were plotted to guide the eye as dashed lines (10 MKS and a bolometric Bond albedo of 0.69). The selection of this albedo and thermal inertia was somewhat arbitrary, but they are in keeping with values observed across Tethys' leading hemisphere. As the figure shows between longitudes $\sim 220^\circ$ W and 160° W even the best-fitting diurnal curves are unable to fully reproduce the shape and values of the morning temperature warming curve (but notably the models are able to fit the nighttime temperatures). Between 220° and 200° W this effect is so severe that there are considered to be no adequate fits to the data. One possible explanation is that our diurnal temperature model is not adequately accounting for the effect of macroscopic surface roughness. Rozitis and Green (2011) showed that the observed temperatures of a rough surface could vary by > 150 K depending upon the viewing geometry on an airless body (although we note this number was derived for an asteroid-like surface, which was assumed to have a lower albedo and higher thermal inertia than Tethys). While such

temperature differences are well above those observed here it may be that roughness could explain the shape difference between the warming curves predicted and the temperatures observed. One thing to note however is that roughness effects are expected to be most pronounced at high emission angles, where sloping surfaces with temperatures potentially differing from the average local temperature are preferentially visible, which isn't the case with these observations (see Fig. 6). For instance, observations at 190° W, 10° N at local times 110–190, where the discrepancy relative to the model is severe, all have emission angles $< 40^\circ$. However, the region of the discrepancy ($\sim 160^\circ$ to 220° W) is one of the areas preferentially bombarded by E ring grains (Fig. 1, Kempf et al., 2018). One possible explanation is that this sand-blasting and subsequent recoating of the surface has increased its roughness so much that roughness effects are being observed even at small emission angles. During Rev 214 the longitude of the sub-solar point increases from 131 to 202° W, while the sub-spacecraft longitude increases between 153 and 222° W (i.e. the sub-spacecraft longitude is about 20° west of the sub-solar longitude for much of the flyby). Therefore if the terrain were very rough around the sub-Saturn point (180° W), then CIRS would be viewing either warm sun-facing slopes, or cool shaded ones. This viewing geometry would produce a very different warming curve than if the same surface were observed at nadir. The current thermal model is unable to account for roughness variations (although we note that some thermal models can account for them e.g. Abramov et al., 2013; Piqueux and Christensen, 2011). If the temperatures we derived from the CIRS data are too high (i.e. the surface is rough enough that warm slopes are being preferentially observed), then the

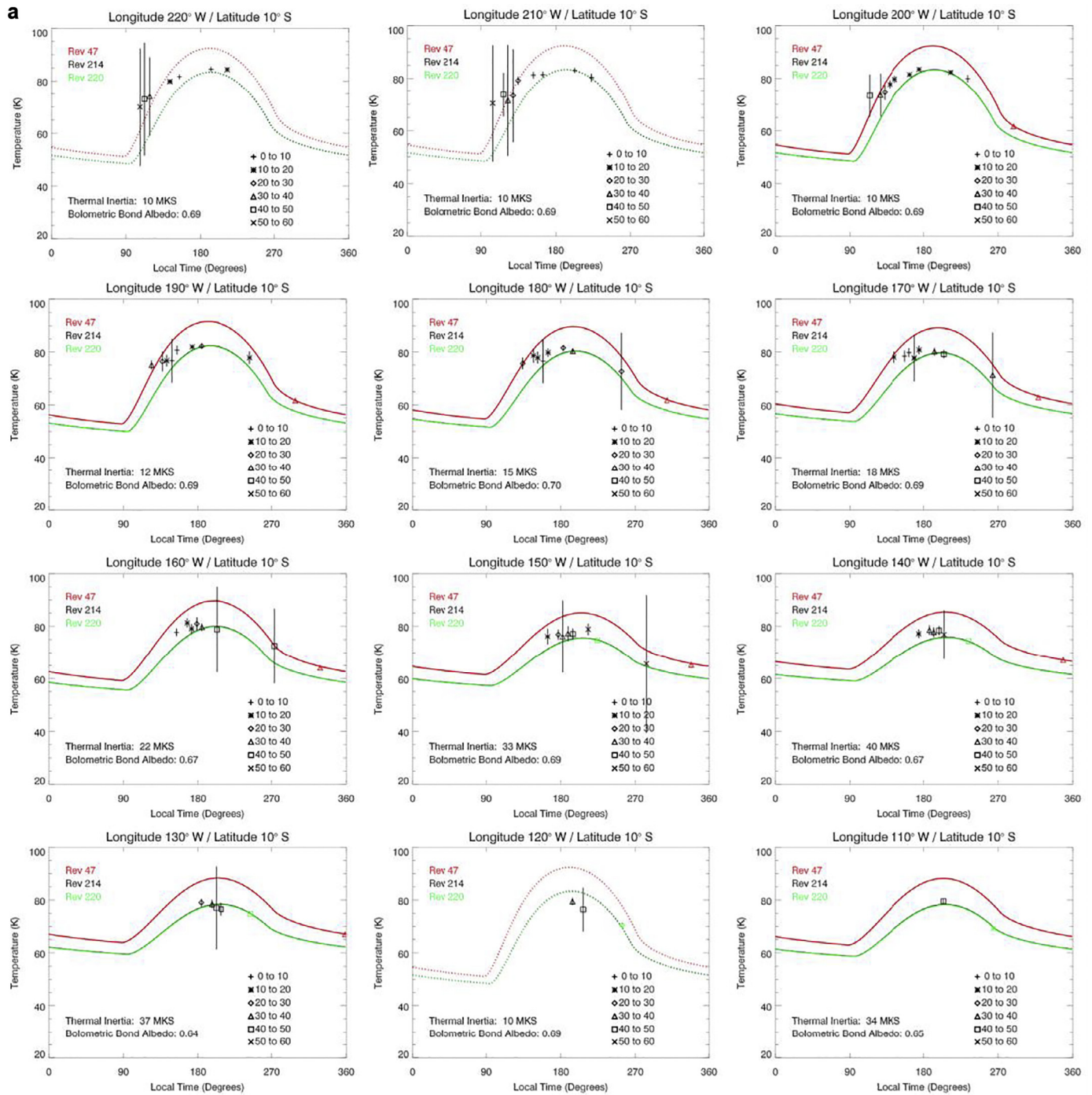


Fig. 6. Best fit diurnal temperature curves compared to observed local time temperatures for different longitudes along latitudes 10° S, 0° N and 10° N. Observations and modeled temperatures for different epochs are given by different colors, and the symbol of the observed temperatures describes its emission angle (see key in figure for details). The best fitting thermal inertia and bolometric Bond albedo for each longitude and latitude location is given in the figure. In the event an acceptable fit wasn't found the diurnal curves produced by the best fit to 200° W, 10° S (thermal inertia of 10 MKS and a bolometric Bond albedo of 0.69) are shown to guide the eye (given by the dotted lines). Since Rev 214 and 220 occur closer together than Rev 47 their modeled diurnal temperature curves are almost the same. (a) Diurnal curves comparing the observed local time temperatures for different longitudes along latitude 10° S. (b) Diurnal curves comparing the observed local time temperatures for different longitudes along latitude 0° N. (c) Diurnal curves comparing the observed local time temperatures for different longitudes along latitude 10° N. (For interpretation of the references to color in this figure legend, the reader is referred to the web version of this article.)

thermal inertia derived from them could also be higher (and/or the albedo lower).

Table 2 directly compares Tethys' bolometric Bond albedo and thermal inertias derived in this work with those derived by Howett et al. (2012). Only two of the three regions investigated by Howett et al. (2012) are covered in this study, but the results show that

the albedos at both of these locations (inside the anomaly and across the boundary region) agree within the uncertainties. The tabulated results also show that the thermal inertias derived here and by Howett et al. (2012) agree within the uncertainties in the boundary region, but the thermal inertia values derived here for the region inside the thermal anomaly are higher but have a slightly larger spread of

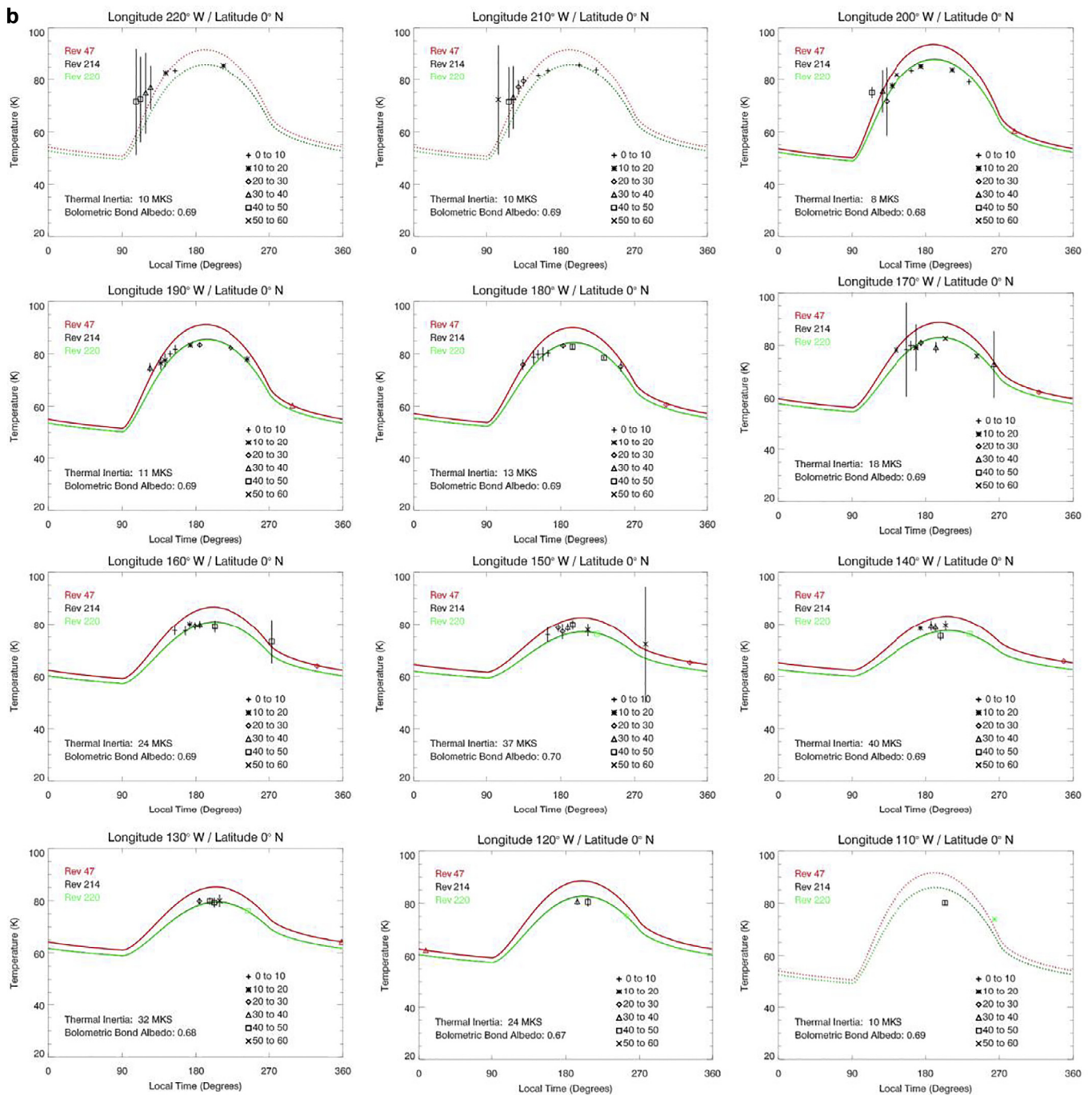


Fig. 6. (continued)

values (37 ± 6 MKS compared to 25 ± 3 MKS). This difference is small (3 MKS if the uncertainties are considered), but is not understood. We note that the main difference between the two studies is the daytime temperatures used to constrain the thermophysical properties (Howett et al., (2012) used Rev 47 nighttime data too).

The comparison of these results to those previously published ones continues in Fig. 7, which compares all the mapped thermal inertia and bolometric Bond albedo values to those inside the thermally anomalous regions of Mimas, Tethys and Dione (Howett et al., 2011; 2012, 2014). The figure further illustrates points already discussed: the bolometric Bond albedo of Tethys’ surface is not uniform inside the anomalous region, and the thermal inertia inside the anomaly is higher than its surroundings. The figure also shows that the thermal inertia of Tethys inside the anomalous region is higher than previously published values

in multiple locations, not just in the Howett et al. (2012) region described above. It also shows that thermal inertia on Tethys does not exceed those on Mimas, but always exceeds those on Dione. So this observation supports the notion that the magnitude of Tethys’ thermal anomaly is between that of Mimas and Dione. Fig. 7 shows how the thermal inertia and bolometric Bond albedo values change with longitude. It’s a little difficult to see any patterns in their variation, other than noting that thermal inertia in the anomalous region increases from 180° W to ~140° W.

4. Conclusions

Maps of thermal inertia and bolometric Bond albedo have been successfully produced using Cassini CIRS data. The results confirm the

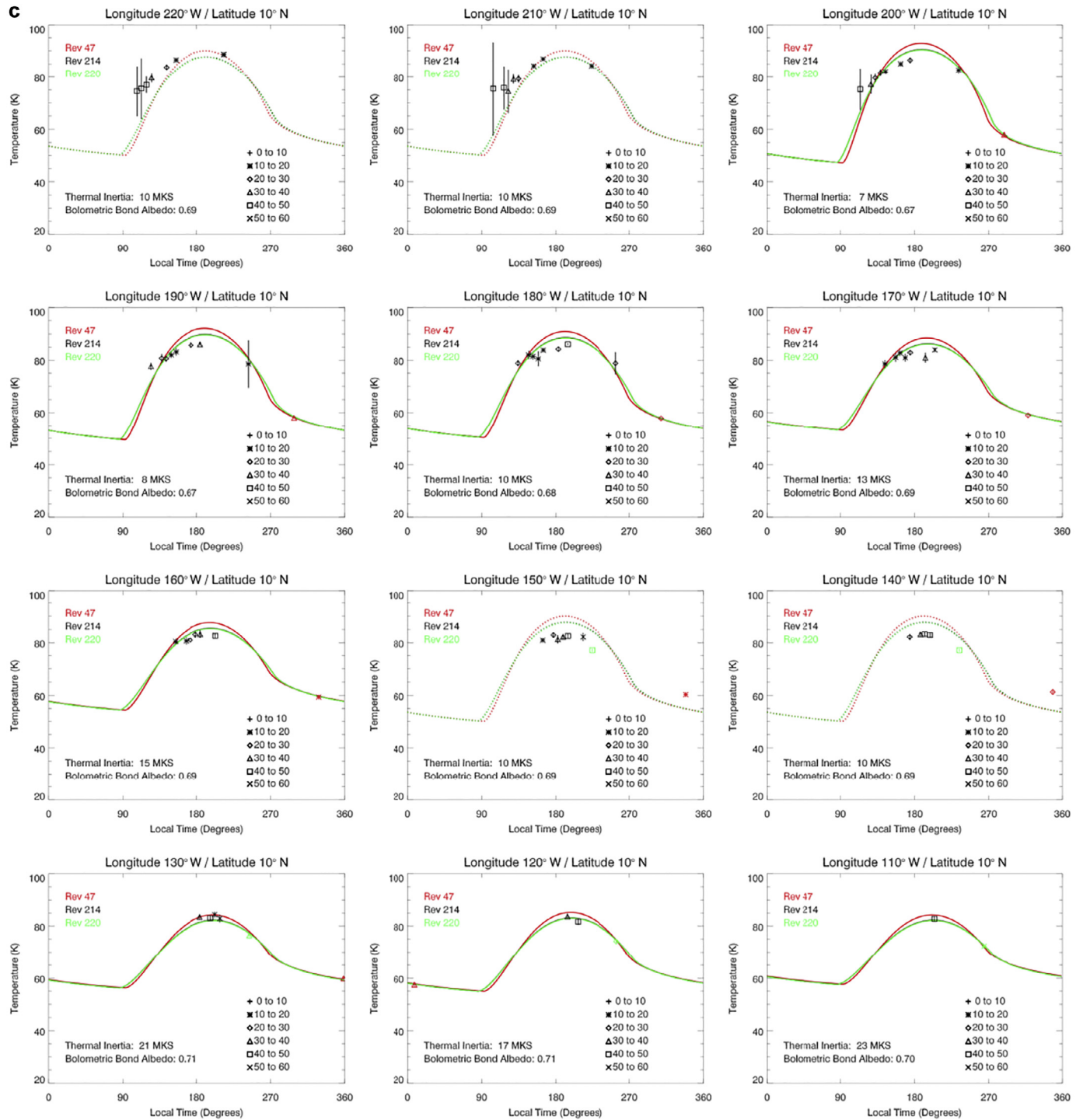


Fig. 6. (continued)

Table 2

Comparison of the bolometric Bond albedo and thermal inertia determined in Howett et al. (2012) and those found in this work.

	Bin 1 (Outside the Anomaly)	Bin 2 (Across the Anomaly boundary)	Bin 3 (Inside of the Anomaly)
Longitude Coverage	210° W to 220° W	175° W to 185° W	140° W to 150° W
Latitude Coverage	5° S to 5° N	5° S to 5° N	5° S to 5° N
Albedo (Howett et al., 2012)	0.67 ± 0.01	0.68 ± 0.01	0.66 ± 0.01
Albedo (This study)	–	0.69 ± 0.01	0.69 ± 0.01
Thermal Inertia (H12)	5 ± 1	11 ± 1	25 ± 3
Thermal Inertia (This study)	–	14 ± 2	37 ± 6

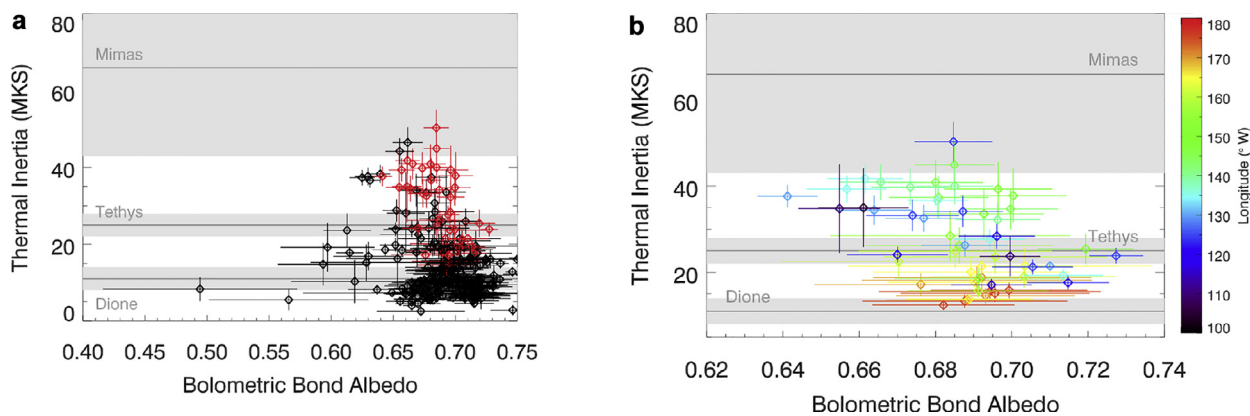


Fig. 7. Bolometric bond albedo variation with thermal inertia for different surface regions and the $\pm 1\sigma$ uncertainty. In all subfigures the previously published thermal inertia inside the thermal anomalies of Mimas, Tethys and Dione are indicated by the grey lines, and their uncertainties by the grey shading (c.f. Howett et al., 2011, 2012 and 2014). (a) Bolometric Bond albedo variation with thermal inertia for all points across Tethys, the red points indicate regions on Tethys' leading hemisphere that are within $\pm 20^\circ$ latitude of the equator (i.e. the nominal "PacMan" region). (b) Bolometric Bond albedo variation with thermal inertia for all values on Tethys' leading hemisphere within $\pm 20^\circ$ latitude of the equator (i.e. the nominal "PacMan" region", and shown in red in subfigure (a)). The color of the points indicate longitude, as given by the key. (For interpretation of the references to color in this figure legend, the reader is referred to the web version of this article.)

presence of a thermally anomalous region on Tethys' leading hemisphere, as first described by Howett et al. (2012). The anomalous region is confirmed to be lens-shaped, on the leading hemisphere, and extends in latitude from $\sim \pm 20^\circ$. These maps, along with cross-sections of thermal inertia and bolometric Bond albedo variations with longitude (produced for a variety of latitudes), show small-scale variations in their values. Perhaps most significantly the thermal inertia and bolometric Bond albedo from longitudes $\sim 160^\circ$ W to 100° W show a general north-south asymmetry: with thermal inertia increasing from northern to southern latitudes, while albedos increase from southern to northern ones. At all latitudes (except the equator and 10° S), thermal inertia increases towards the center of Tethys' leading hemisphere. Bolometric Bond albedos at different latitudes on Tethys' trailing hemisphere show good agreement, while those on the leading hemisphere differ but all appear to decrease away from 180° W. The reason for these albedo and thermal inertia differences is unclear, but could be due to variations in the balance between surface modification by E ring grains and high-energy electrons which both bombard this hemisphere albeit with different bombardment patterns.

Acknowledgment

The authors would like to thank NASA's Cassini project for funding this work, and Liebovitch (1974) for analysis inspiration.

Supplementary materials

Supplementary material associated with this article can be found, in the online version, at doi:10.1016/j.icarus.2018.12.018.

References

Abramov, O., Rathbun, J.A., Schmidt, B.E., Spencer, J.R., 2013. Detectability of thermal signatures associated with active formation of 'chaos terrain' on Europa. *Earth Planet. Sci. Lett.* 384, 37–41.

Acton, C., 1996. Ancillary data services of NASA's navigation and ancillary information facility. *Planet. Space Sci.* 44, 65–70.

Buratti, B., Veverka, J., 1984. Voyager Photometry of Rhea, Dione, Tethys, Enceladus and Mimas. *Icarus* 58, 254–264.

Elder, C., Helfenstein, P., Thomas, P., Veverka, J., Burns, J.A., Denk, T., Porco, C., 2007. Tethys' mysterious equatorial band. *Bull. Am. Astron. Soc.* 39, 429.

Filacchione, G., D'Aversa, E., Capaccioni, F., Clark, R.N., Cruikshank, D.P., Ciarniello, M., Cerroni, P., Bellucci, G., Brown, R.H., Buratti, B.J., Nicholson, P.D., Jaumann, R., McCord, T.B., Sotin, C., Stephan, K., Dalle Ore, C.M., 2016. Saturn's icy satellites investigated by Cassini-VIMS. IV. Daytime temperature maps. *Icarus* 271, 292–313.

Flasar, F.M., Kunde, V.G., Abbas, M.M., Achterberg, R.K., Ade, P., Barucci, A., Bézard, B., Bjoraker, G.L., Brasunas, J.C., Calcutt, S.B., Carlson, R., Césarsky, C.J., Conrath, B.J.,

Coradini, A., Courtin, R., Coustenis, A., Edberg, S., Edgington, S., Ferrari, C., Fouchet, T., Gautier, D., Gierasch, P.J., Grossman, K., Irwin, P., Jennings, D.E., Lellouch, E., Mamoutkine, A.A., Marten, A., Meyer, J.P., Nixon, C.A., Orton, G.S., Owen, T.C., Pearl, J.C., Prangé, R., Raulin, F., Read, P.L., Romani, P.N., Samuelson, R.E., Segura, M.E., Showalter, M.R., Simon-Miller, A.A., Smith, M.D., Spencer, J.R., Spilker, L.J., Taylor, F.W., 2004. Exploring the Saturn system in the thermal infrared: the composite infrared spectrometer. *Space Sci. Rev.* 115, 169–297. <https://doi.org/10.1007/s11214-004-1454-9>.

Hamilton, D.P., Burns, J.A., 1994. Origin of Saturn's E ring: self-sustained, naturally. *Science* 264, 550.

Hendrix, A.R., Filacchione, G., Paranicas, C., Schenk, P., satellites, Icy Saturnian, 2018. Disk-integrated UV-IR characteristics and links to exogenic processes. *Icarus* 300, 103–114.

Howett, C.J.A., Spencer, J.R., Schenk, P., Johnson, R.E., Paranicas, C., Hurford, T.A., Verbiscer, A., Segura, M., 2011. A high-amplitude thermal inertia anomaly of probable magnetospheric origin on Saturn's moon Mimas. *Icarus* 216, 221–226. <https://doi.org/10.1016/j.icarus.2011.09.007>.

Howett, C.J.A., Spencer, J.R., Hurford, T., Verbiscer, A., Segura, M., returns, PacMan, 2012. An electron-generated thermal anomaly on Tethys. *Icarus* 221, 1084–1088.

Howett, C.J.A., Spencer, J.R., Hurford, T., Verbiscer, A., Segura, M., 2014. Thermophysical property variations across Dione and Rhea. *Icarus* 241, 239–247.

Howett, C., Spencer, J., Pearl, J., Segura, M., 2010. Thermal inertia and bolometric Bond albedo values for Mimas, Enceladus, Tethys, Dione, Rhea and Iapetus as derived from Cassini/CIRS measurements. *Icarus* 206, 573–593.

Kempf, S., Horányi, M., Hsu, H.W., Hill, T.W., Juhász, A., Smith, H.T., 2018. Saturn's diffuse E ring and its connection with Enceladus. in: *Enceladus*. University of Arizona Press.

Liebovitch, L.S., 1974. Discovery of a new radiation source Z-1 in Taurus. *Q. J. R. Astron. Soc.* 15, 141–145.

Nelder, J.A., Mead, R., 1965. A simplex method for function minimization. *Comput. J.* 7, 308–313.

Paranicas, C., Roussos, E., Decker, R.B., Johnson, R.E., Hendrix, A.R., Schenk, P., Cassidy, T.A., Dalton III, J.B., Howett, C.J.A., Kollmann, P., Patterson, W., Hand, K.P., Nordheim, T.A., Krupp, N., Mitchell, D.G., 2014. The lens feature on the inner Saturnian satellites. *Icarus* 234, 155–161.

Piqueux, S., Christensen, R.P., 2011. Temperature-dependent thermal inertia of homogeneous Martian regolith. *J. Geophys. Res.* 116, E07004.

Rozitis, B., Green, S.F., 2011. Directional characteristics of thermal-infrared beaming from atmosphereless planetary surfaces – a new thermophysical model. *Mon. Not. R. Astron. Soc.* 415, 2042–2062.

Schenk, P.D.P., Hamilton, Johnson, R.E., McKinnon, W.B., Paranicas, C., Schmidt, J., Showalter, M.R., 2011. Plasma, plumes and rings: Saturn system dynamics as recorded in global color patterns on its midsize icy satellites. *Icarus* 211, 740–757. <https://doi.org/10.1016/j.icarus.2010.08.016>.

Schaible, M.J., Johnson, R.E., Zhigilei, L.V., Piqueux, S., 2017. High energy electron sintering of icy regoliths: formation of the PacMan thermal anomalies on the icy Saturnian moons. *Icarus* 285, 211–223.

Shkuratov, Y.G., Helfenstein, P., 2001. The opposition effect and the quasi-fractal structure of regolith: I. theory. *Icarus* 152, 96–116.

Spencer, J.R., 1989. A rough-surface thermophysical model for airless planets. *Icarus* 83, 27–38. [https://doi.org/10.1016/0019-1035\(90\)90004-5](https://doi.org/10.1016/0019-1035(90)90004-5).

Spencer, J.R., 1999. Temperatures on Europa from Galileo PPR: nighttime thermal anomalies. *Science* 284, 1514–1516.

Stooke, P.J., 1989. Tethys: volcanic and structural geology. *Lunar Planet. Sci.* 20, 1071.

Stooke, P.J., 2002. Tethys and Dione: new geological interpretations. *Lunar Planet. Sci.* 33, 1553.

Verbiscer, A., French, R., Showalter, M., Helfenstein, P., 2007. Enceladus: cosmic Graffiti artist caught in the act. *Science* 315, 815.